Mesoscale evolution of non-graphitizing pyrolytic carbon in aligned carbon nanotube carbon matrix nanocomposites

Citation: Stein, Itai Y., Ashley L. Kaiser, Alexander J. Constable, Luiz Acauan, and Brian L. Wardle. "Mesoscale Evolution of Non-Graphitizing Pyrolytic Carbon in Aligned Carbon Nanotube Carbon Matrix Nanocomposites." Journal of Materials Science 52, no. 24 (August 22, 2017): 13799–13811.

As Published: http://dx.doi.org/10.1007/s10853-017-1468-9

Publisher: Springer-Verlag

Persistent URL: http://hdl.handle.net/1721.1/115056

Version: Author's final manuscript: final author's manuscript post peer review, without publisher's formatting or copy editing

J Mater Sci manuscript No.
(will be inserted by the editor)

Meso-scale evolution of non-graphitizing pyrolytic carbon in aligned carbon nanotube carbon matrix nanocomposites

Itai Y. Stein, Ashley L. Kaiser, Alexander J. Constable, Luiz Acauan, and Brian L. Wardle

Received: date / Accepted: date

Abstract Polymer-derived pyrolytic carbons (PyCs) are highly desirable building blocks for high strength low density ceramic meta-materials, and reinforcement with nanofibers is of interest to address brittleness and tailor multi-functional properties. The properties of carbon nanotubes (CNTs) make them leading candidates for nanocomposite reinforcement, but how CNT confinement influences the structural evolution of the PyC matrix is unknown. Here, the influence of aligned CNT proximity interactions on nano- and meso-scale structural evolution of phenol-formaldehyde derived PyCs is established as a function of pyrolysis temperature (T_p) using x-ray diffraction, Raman spectroscopy, and Fourier transform infrared spectroscopy. Aligned CNT PyC matrix nanocomposites are found to evolve faster at the meso-scale by plateauing in crystallite size at $T_p \sim 800°C$, which is more than 200°C below that of unconfined PyCs. Since the aligned CNTs used here exhibit $\sim$ 80 nm average separations and $\sim$ 8 nm diameters, confinement effects are surprisingly not found to influence PyC structure on the atomic-scale at $T_p \leq 1400°C$. Since CNT confinement could lead to anisotropic crystallite growth in PyCs synthesized below $\sim 1000°C$, and recent modeling indicates that more slender crystallites increase PyC hardness, these results inform fabrication of PyC-based meta-materials with unrivaled specific mechanical properties.

Keywords Carbon nanotubes (CNTs) · Pyrolysis · Nanocomposites · Polymer derived ceramics · X-ray diffraction (XRD) · Raman spectroscopy · Fourier transform infrared (FTIR) spectroscopy

I. Y. Stein, L. Acauan, and B. L. Wardle
Department of Aeronautics and Astronautics
Massachusetts Institute of Technology
Cambridge, MA 02139, USA
E-mail: iys@alum.mit.edu; wardle@mit.edu

I. Y. Stein
Department of Mechanical Engineering
Massachusetts Institute of Technology
Cambridge, MA 02139, USA

A. L. Kaiser, A. J. Constable
Department of Materials Science and Engineering
Massachusetts Institute of Technology
Cambridge, MA 02139, USA

A. L. Kaiser
Department of Chemical Engineering
University of Massachusetts Amherst
Amherst, MA 01003, USA

A. J. Constable
Department of Materials Science and Engineering
The Pennsylvania State University
University Park, PA 16801, USA

Introduction

Nano-architected ceramic meta-materials, especially those made from additively manufactured polymer derived ceramics [1–3], have great potential for next-generation strong and ultra-lightweight structural materials due to their high specific strength and stiffness [1–9]. But the application of these meta-materials is hindered by the inherently brittle and flaw-sensitive ceramics that comprise their building blocks [9]. Although ceramic nano-composites were previously shown to exhibit significantly enhanced toughness compared to the pure ceramic matrix [10–12], limitations of current generation 3D printing techniques [1, 13] have caused these advancements to have little impact on the ceramic meta-materials studied previously [1–9]. Recent work on nano-

architected ceramic materials made from polymer derived pyrolytic carbon (PyC), coupled with extensive previous work showing that nanofiber (NF) reinforced polymer matrix nano-composites can exhibit enhanced stiffness and ductility [14–16], indicate that meta-materials could soon be fabricated using NF reinforced ceramic nano-composites with enhanced mechanical properties [17–19]. However, since the nano-, meso-, and micro-scale structure of the PyC matrix strongly influences the mechanical behavior of the ceramic nano-composites, but not much is currently known about the impact of NF proximity on the graphitic crystallite formation and self-organization processes, in this report we quantify the evolution of NF-confined graphitic crystallites in PyC matrix nano-composites as a function of the pyrolysis temperature (T_p).

The theoretical physical properties, in combination with their ability to be produced in large industrial scales [23, 24], has motivated the previous exploration of carbon nanotubes (CNTs) as NF reinforcement in polymer matrix nano-composites in both aligned [25–29] and randomly oriented [29–33] morphologies. Because CNT alignment can take full advantage of the anisotropic mechanical properties of the CNTs [23, 34], and also facilitates the polymer infusion process [35, 36], e.g., through capillary-assisted wetting, the polymer derived ceramics studied here consist of aligned CNT PyC matrix nano-composites (A-CMNCs). See Fig. 1a for a multi-scale illustration of the A-CMNC structure. Since the chemistry in the polymeric matrix precursors strongly influences the processing conditions and properties of the resulting PyC matrix in the A-CMNCs [37–40], to ensure that the A-CMNCs studied here are directly applicable to polymer derived ceramic meta-materials, the polymer resin utilized to synthesize the precursor nano-composites had to both be compatible with additive manufacturing techniques (e.g., photoresists) and yield a stiff and lightweight PyC.

Two polymeric precursors commonly utilized for the synthesis of PyCs include polyacrylonitrile (PAN) and phenol-formaldehyde (P-F), both of which yield non-graphitizing PyCs, as coined by Franklin in the 1950s [37], that are characterized by smaller graphitic crystallites that exhibit significant disorder, lack a preferential alignment direction, and enclose randomly-shaped meso-scale pores [37–40]. Although the influence of CNT confinement on the structural evolution of PAN during pyrolysis was previously studied in detail [41–47], and it was found that CNTs may [41–43] or may not [44–47] help facilitate graphitization at $T_p < 1500°C$, not much is currently known about how CNTs impact the graphitic crystallite growth and self-organization in P-F composites. A recent report has explored the impact of CNT confinement on the pyrolyzation of P-F [48], but this study did not report the evolution of the three common measures that normally characterize the graphitic crystallites that comprise the PyCs [49–54]: the crystallite size (L_a) originating from the (100) and (110) 3D lattice planes (*i.e.*, *via* the [100] and [110] Miller indices also known as $hk\ell$); the crystallite thickness (L_c) originating from the (002) lattice plane (*i.e.*, *via* the [002] $hk\ell$); and the inter-layer separation of the (002) lattice

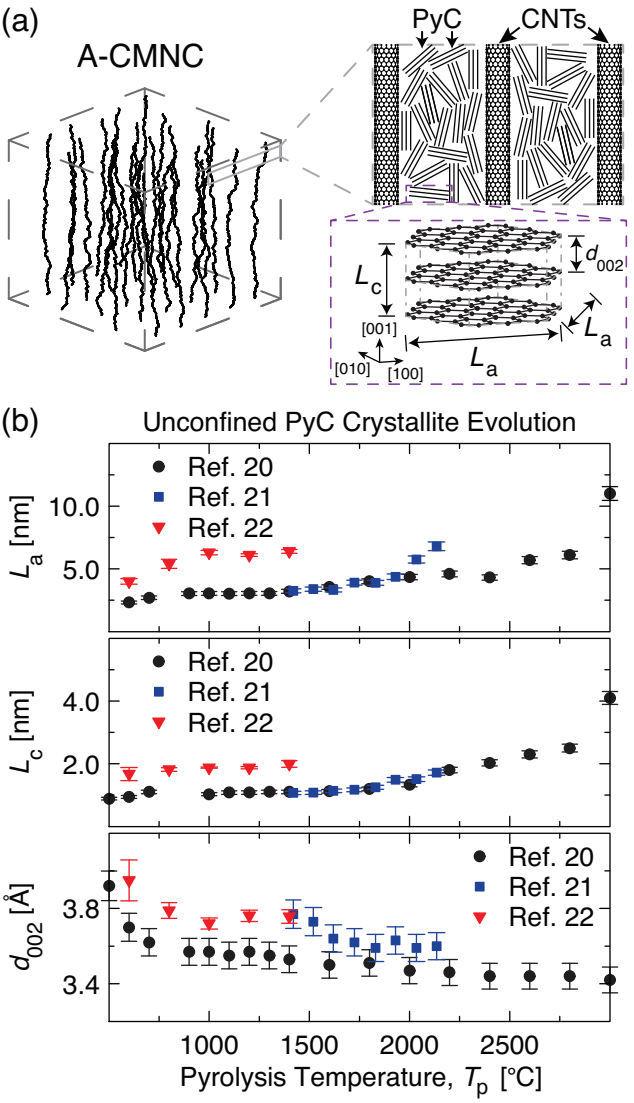

Fig. 1 Illustration of the aligned carbon nanotube (CNT) pyrolytic carbon (PyC) matrix nanocomposite (A-CMNC) structure. (a) Three-dimensional and cross-sectional representation of the CNT and graphitic crystallite arrangement in A-CMNCs, and the geometric measures used to quantify the size (L_a), thickness (L_c), and inter-layer separation (d_{002}) of the graphitic crystallites. (b) Previously reported L_a, L_c, and d_{002} for non-graphitizing PyCs undergoing pyrolysis at temperatures up to 3000°C showing that significant crystallite evolution does not typically occur in heat treatments preformed below ∼ 2000°C [20–22].

planes (d_{002}). See the inset of Fig. 1a for an illustration of the L_a, L_c, and d_{002} that define the graphitic crystallites, and Fig. 1b for their evolution in pure P-F undergoing pyrolysis up to $T_p \sim 3000°C$ [20–22]. Because many P-F resins are commercially available as ultraviolet curable photoresists [55], such as the broadly utilized SU8 photoresist, and typically yield PyCs with low densities ($\lesssim 1.2$ g/cm^3) and high hardness ($\gtrsim 4$ GPa) [22], they are well-suited for additive manufacturing of next-generation polymer derived ceramic metamaterials. This means that elucidation of the influence of CNT confinement on the nano-, meso-, and micro-scale evolution of the P-F during pyrolysis at temperatures typical of additive manufacturing processes (*i.e.*, $T_p \lesssim 1500°C$ [1–3]) is necessary, and in this report we use in-depth morphological, structural, and chemical information to quantify how aligned CNTs impact the graphitic crystallite growth and self-organization in the PyC matrix of A-CMNCs.

Methods

Synthesis and processing techniques

Aligned CNT arrays were grown in a 22 mm internal diameter quartz tube furnace at atmospheric pressure *via* a thermal catalytic chemical vapor deposition process, very similar to a previously described process with ethylene as the carbon source and water vapor added to the inert gas [56–58]. The CNTs were grown on 1 cm × 1 cm Si substrates forming aligned CNT arrays that are up to ∼ 1 mm tall, and are composed of multiwalled CNTs that have an average outer diameter of ∼ 8 nm ($3-7$ walls with an inner diameter of ∼ 5 nm and intrinsic CNT density of ∼ 1.6 g/cm^3) [36, 58], inter-CNT spacing of $\sim 70-80$ nm [59–62], and V_f of ∼ 1% CNTs [58]. A post-growth H_2 anneal [63] is used to weaken the attachment of the CNTs to the catalyst layer, which enables the easy delamination of the CNT array from the Si substrate using a standard lab razor blade, thereby allowing further CNT processing to be performed in their free-standing state.

Fabrication of P-F polymer precursors *via* vacuum assisted wetting was performed by first gently depositing free-standing CNT arrays into hollow cylindrical Al molds, ensuring that the primary axis of the CNTs was orthogonal to the plane of the mold. The CNT array was then infused with a de-gassed phenolic resin (Durite SC-1008, Momentive Specialty Chemicals, Inc.) at 40°C under vacuum for ∼ 24 hr to allow the highly viscous P-F resin sufficient time to infiltrate the inter-CNT space before curing to form the polymeric nanocomposite precursors to the A-CMNCs [36, 64, 65]. This 24 hr vacuum infusion step also enabled the majority of air trapped in the P-F resin as it flowed into the inter-CNT space to be removed, which thereby minimized the porosity of the P-F matrix in the polymeric nanocomposite precursors. The pure P-F and polymer nanocomposite precursors were then cured for 6 hr at 80°C under vacuum [36, 64, 65]. These P-F polymer nanocomposite precursors to the A-CMNC preserve the original V_f of the aligned CNT arrays (*i.e.*, ∼ 1 vol. % CNTs and ∼ 99 vol. % P-F resin), and since the density of the P-F resin is $\sim 1.1 \pm 0.1$ g/cm^3, this corresponds to a CNT mass fraction of $\sim 1.5 \pm 0.1$ wt. % (and P-F mass fraction of $\sim 98.5 \pm 0.1$ wt. %, respectively). See Sec. S1 in the Supplementary Materials for an illustration of the PyC and A-CMNC polymeric precursor synthesis approach.

The polymer precursor samples were then heat treated to transform the P-F resin into pyrolytic carbon (PyC). Pyrolysis was performed using a commercial hot wall tube furnace (STT-1600, from SentroTech Corp.) with a 3.5 in inner diameter SiC tube in an Ar environment at a ramp rate of 4°C/min (furnace maximum) at the following T_p and hold times (t_{hold}) of $t_{hold} = 30$ min (See Sec. S1 in the Supplementary Materials for illustration): 600°C, 800°C, 1000°C, 1200°C, and 1400°C. An alumina boat was used to ensure that the prepared PyC samples exhibited minimal curvature post-pyrolysis. See Sec. S2 in the Supplementary Materials for electron microscopy characterization of the cross-sectional morphology of PyCs and A-CMNCs synthesized at $600°C \leq T_p \leq 1400°C$.

XRD analysis

To calculate the average effective L_a, L_c, and d_{002} of the graphitic crystallites that comprise the PyCs, the (100) and (002) peaks of the XRD pattern are used in conjunction with the Scherrer equations and Bragg's law as follows [51–54]:

$$L_a = \frac{1.84\lambda_{xrd}}{\beta_{100}\cos(\theta_{100})} \tag{1}$$

$$L_c = \frac{0.89\lambda_{xrd}}{\beta_{002}\cos(\theta_{002})} \tag{2}$$

$$n_{xrd}\lambda_{xrd} = 2d_{002}\sin(\theta_{002}) \tag{3}$$

where λ_{xrd} is the wavelength of the incident x-ray radiation, β_{002} and β_{100} are the full width at half maximum of the (002) and (100) peaks, θ_{002} and θ_{100} are the positions of the (002) and (100) peaks, and n_{xrd} is an integer that corresponds to the number of (002) layers the incident radiation traveled before being reflected

($\rightarrow n_{\mathrm{xrd}} = 1$ is normally assumed) [66]. Since the peak position and full width at half maximum of the (110), θ_{110} and β_{110}, can also be used in Eq. 1 (*i.e.*, instead of θ_{100} and β_{100}, respectively) to yield an independent and supplemental approximation of L_{a} [53], here the L_{a} values we reported are an average of the ones estimated using the (100) and (110) peaks.

A PANalytical X'Pert Pro XRD system was used to analyze samples post-pyrolysis. Cu K_α radiation was passed through a 2° anti-scattering slit with a 0.04 rad Soller slit in X'celerator mode. The XRD experiment was performed at 45 kV and 40 mA with a scanning step interval of 0.02° ($2\theta_{\mathrm{xrd}}$). LaB_6 was used as the standard material for all measurements. The calculated values of L_{a} (*via* Eq. 1), L_{c} (*via* Eq. 2), and d_{002} (*via* Eq. 3) are presented in Table S1 (see Sec. S3, Supplementary Materials), and originate from at least 3 samples at each T_{p}.

Raman spectroscopy analysis

Raman spectra were collected using a LabRam HR800 Raman microscope (Horiba Jobin Yvon) with 532 nm (2.33 eV) laser excitation through a 50× objective (N.A. 0.75). Several spots on each sample (for at least 3 samples at each T_{p}) were studied to ensure that representative data was used when calculating the intensity ($I_{\mathrm{D}}/I_{\mathrm{G}}$) and area ($A_{\mathrm{D}}/A_{\mathrm{G}}$) ratios of the D- and G-bands of the Raman spectra. To facilitate the analysis of the defect information provided by Raman spectroscopy, the Raman spectra were fit using two Lorentzian distributions corresponding to the graphitic D-band (centered at $\omega_{\mathrm{D}} \sim 1350$ cm^{-1}) and amorphous carbon (a-C) G-band (centered at $\omega_{\mathrm{G,a-C}} \sim 1500$ cm^{-1}) [50, 67, 68], and Breit-Wigner-Fano distribution that corresponds to the graphitic G-band (centered at $\omega_{\mathrm{G}} \sim 1590$ cm^{-1}) [69–71]. The fitting expression detailed in Sec. S4 (Supplementary Materials) yielded excellent agreement (coefficients of determination $\mathbb{R}^2 > 0.99$) with the experimental Raman spectra at 1000 cm$^{-1} \leq \omega \leq 1800$ cm^{-1}, and $I_{\mathrm{D}}/I_{\mathrm{G}}$ was evaluated simply using the I_{D} and I_{G} from the Lorentzian and BWF fits of the D- and G-bands, while $A_{\mathrm{D}}/A_{\mathrm{G}}$ was evaluated using the areas of the Lorentzian and BWF fits of the D- and G-bands (A_{D} and A_{G}, respectively). See Sec. S4 (Supplementary Materials) for additional details.

FTIR analysis

FTIR spectroscopy was performed using a FTIR6700 Fourier Transform Infrared Spectrometer (Thermo Fisher Scientific, Inc.), and the chemical structure was analyzed using the OMNIC software (Thermo Fisher Scientific, Inc.). The attenuated total reflection mode technique was used to study the chemistry of a cured phenolic resin baseline, and the KBr pellet method was employed in transmission mode. All FTIR signal was transformed to absorbance mode during the analysis. An average of 64 scans with a resolution of 8 cm^{-1} were taken for each sample, and 3 samples were tested at each T_{p}.

Results and discussion

Graphitic crystallite geometry evolution

Crystallite geometry in carbon materials is commonly approximated using the effective L_{a}, L_{c}, and d_{002} that are evaluated from their x-ray diffraction (XRD) patterns [52–54]. See Fig. 2 for the XRD patterns, and the evaluated L_{a}, L_{c}, and d_{002} as a function of T_{p} (L_{a}, L_{c}, and d_{002} values are summarized in Table S1 in Sec. S3, Supplementary Materials). As shown in Fig. 2a, the diffraction patterns (smoothed using a 32-point moving average) of P-F resin transforming into PyC with (*i.e.*, A-CMNC) and without (*i.e.*, PyC) CNT confinement exhibit three main peaks of interest [72, 73]: the first is observed at $18° \lessapprox 2\theta \lessapprox 22°$ and belongs to the (002) plane; the second is observed at $2\theta \approx 43°$ and belongs to the (100) plane; and the third is observed at $2\theta \approx 78°$ and belongs to the (110) plane. Shifting of the (002) peak and large changes in intensity of the (100) and (110) peaks relative to the (002) peak, especially in the A-CMNC spectra, are indicative of a decrease in average crystallite curvature (*i.e.*, fluctuation of the d_{002}) and a turbostratic stacking order [73]. Turbostratic stacking order is further supported by the evolution of d_{002} as a function of T_{p}, as shown in Table S1 (Sec. S3, Supplementary Materials) and Fig. 2b, which indicate that although d_{002} decreases with T_{p}, d_{002} plateaus at $d_{002} \sim 0.38$ nm and a $d_{002} \lesssim 0.34$ nm value indicative of Bernal (*i.e.*, ABAB) stacked graphite is not observed. Also, as indicated by Fig. 2b, CNT confinement does not lead to measurable reductions in the d_{002} of A-CMNCs, which indicates that the CNTs do not significantly influence the atomic order of the graphitic crystallites that comprise the PyC matrix of the A-CMNCs. This is consistent with previous reports on PAN derived PyCs reinforced with CNTs [44–47]. Additionally, the (002) peak may also be related to both annihilation of native defects and an increase in L_{c} of the graphitic crystallites [73]. These results indicate that while higher T_{p} leads to lower crystallite curvature and disorder, the crystallites are still not truly graphitic

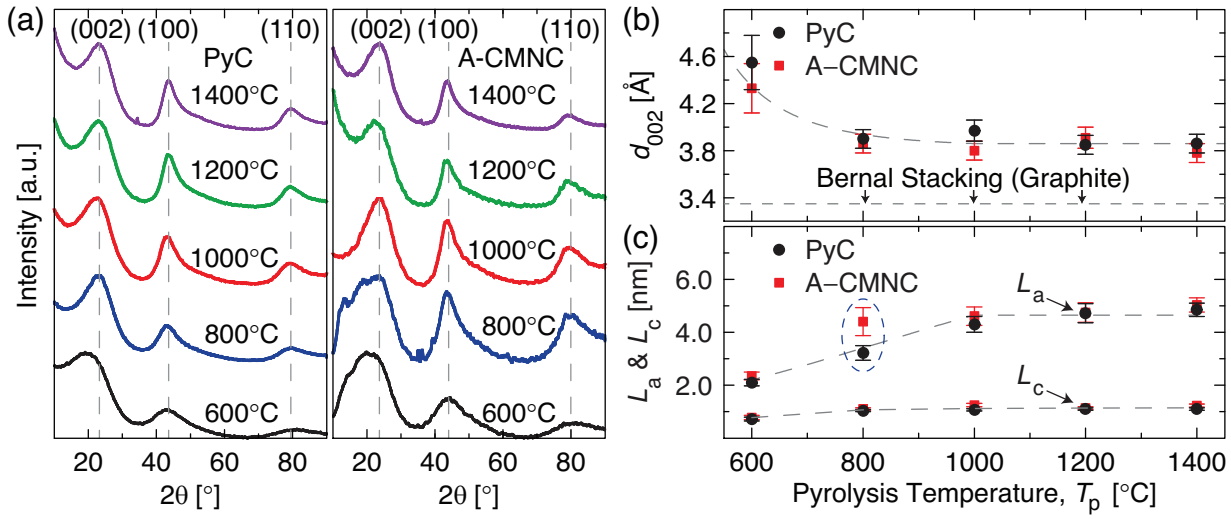

Fig. 2 XRD analysis results for pyrolysis of PyCs and A-CMNCs as a function of the pyrolysis temperature (T_p). (a) Representative XRD patterns showing the evolution of the (002), (100), and (110) peaks as a function of T_p. (b) Inter-layer separation (d_{002}) as a function of T_p showing that CNTs do not lead to a measurable difference in the PyC crystallites at the < 1 nm scale. (c) Crystallite size (L_a) and thickness (L_c) as a function of T_p showing that the A-CMNCs crystallites evolve faster than the PyC crystallites as T_p increases.

in nature, since the (002) peak is at $2\theta < 26.5°$ ((002) peak position for graphite) [52], and that the glassy crystallite arrangement that is expected for P-F undergoing pyrolysis likely holds [39, 55]. Using the (002), (100), and (110) peaks, the geometry of the graphitic crystallites that comprise the PyCs can be studied further.

As Table S1 (Sec. S3, Supplementary Materials) and Fig. 2c illustrate, the L_a of PyCs grows with increasing T_p up to $T_p \sim 1000°C$, and that L_a plateaus at $L_a \sim 5$ nm for $T_p > 1000°C$, which is in good agreement with previous work on P-F undergoing pyrolysis [22]. On the other hand, Fig. 2c illustrates that the L_a of A-CMNCs, which starts at a value similar to that of the PyCs at $T_p \approx 600°C$ ($L_a \sim 2$ nm), grows faster in the $600°C \lessapprox T_p \lessapprox 1000°C$ regime, and reaches the plateau $L_a \sim 5$ value at $T_p \approx 800°C$. This indicates that CNTs facilitate crystallite growth in the [100] and [110] family of directions, which is consistent with previous findings on PAN derived PyCs reinforced with CNTs [42, 43], but that CNT confinement is not sufficient to overcome the large energy barrier that leads to the L_a plateau that subsists until $T_p \gtrsim 2000°C$ [20, 21]. CNT confinement did not have a significant effect on crystallite growth in the [001] family of directions since the L_c of PyCs and A-CMNCs both exhibit slight growth with increasing T_p up to $T_p \sim 800°C$, after which the L_c plateaus at $L_c \sim 1$ nm for $T_p > 800°C$. This is consistent with findings for PAN derived PyCs reinforced with CNTs that show little impact on the L_c evolution with increasing T_p [42–47].

Bonding character evolution

Raman spectroscopy is widely utilized for qualitatively analyzing defect densities and disorder in carbon materials [69, 74–76], and representative Raman spectra for P-F undergoing pyrolysis with (A-CMNCs) and without (PyCs) CNT confinement can be found in Fig. 3. As Fig. 3 shows, the main qualitative evolution of the Raman spectra of PyCs and A-CMNCs is that the D-band, which is normally found at $\sim 1335 - 1350$ cm^{-1} and is representative of defects/disorder in the (002) plane [69, 74–78], is increasing in intensity, while the G-band, which usually found at $\sim 1580 - 1600$ cm^{-1} and corresponds to the in-plane sp^2 bond stretching [69, 74–78], is unchanged. This is confirmed in Fig. 3b, where the intensity (I_D/I_G) and area (A_D/A_G) ratios of the D- and G-bands, which are a common way to discern whether one material/sample is more or less graphitic than another [69, 74, 79, 80], are presented as a function of T_p. The three-band fitting functions that approximated the Raman spectra of PyCs and A-CMNCs (see Fig. 3a), and were subsequently used to evaluate the I_D/I_G and A_D/A_G presented in Fig. 3b can be found in Sec. S4 of the Supplementary Materials. As Fig. 3b illustrates, I_D/I_G increases monotonically as a function of T_p, whereas A_D/A_G is seen to increase up to $T_p \sim 1000°C$ and subsequently decrease as T_p continues to rise. This behavior is related to thermally-activated defect formation and annihilation [81], for example, since the heat introduced during pyrolysis could potentially lead to the formation of new wall defects in the CNTs and/or could enable the native wall defects,

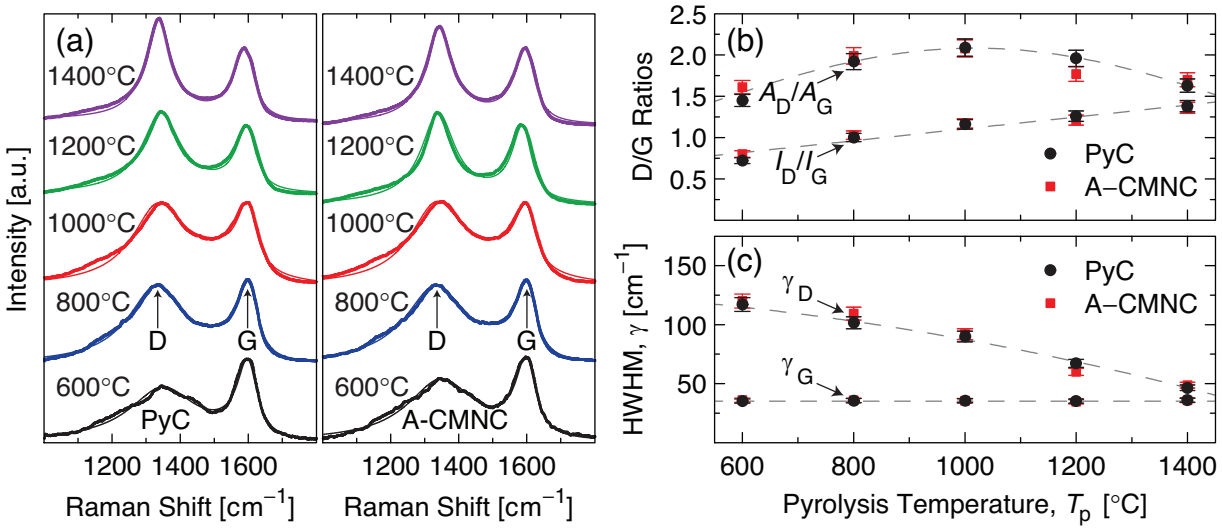

Fig. 3 Raman spectroscopy analysis results for PyCs and A-CMNCs as a function of the pyrolysis temperature (T_p). (a) Representative Raman spectra showing the evolution of the D and G bands as a function of T_p. (b) Evolution of the intensity (I_D/I_G) and area (A_D/A_G) ratios of the D- and G-bands as a function of T_p illustrating that A-CMNCs and PyCs have similar defect densities. (c) Scaling of the half width half maximum of the D-band (γ_D) and G-band (γ_G) as a function of T_p reinforcing that CNTs do not lead to significant changes at the < 1 nm scale.

which were found to be present in significant enough amounts to allow small gas molecules to diffuse through the CNT walls into their inner core [82, 83], to migrate and annihilate [81]. The observed variance in the I_D/I_G and A_D/A_G evolution as a function of T_p is related to their origin from the vibrational density of states, where A_D/A_G better represents the impact of defects when their probability is low while I_D/I_G better represents the modes/vibrations that account for the most resonant Raman processes [84]. This difference illustrates that A_D/A_G is best suited for studying low defect density carbon materials (e.g. CNTs) [84], while I_D/I_G could yield more representative information for highly defective carbon materials (e.g., PyCs) [84], and further emphasizes that the inclusion of both quantities is necessary for composites that contain both types of carbon materials (e.g. A-CMNCs). To help extract further information from the Raman spectra, the half width half maximums of the D- and G-bands (γ_D and γ_G, respectively) need to be evaluated, and can be found in Fig. 3c. As Fig. 3c indicates, γ_D decreases as a function of T_p from $\gamma_D \sim 120$ to 50 cm^{-1}, while γ_G remains constant to within the experimental uncertainty at $\gamma_G \sim 35$ cm^{-1}. This type of behavior is consistent with stage 2 in the three-stage amorphization trajectory originally proposed in Ref. 69, and further explored for defective graphene (Ref. 84) and PyCs (Ref. 71), since Ref. 84 reported $\gamma_G \sim 40$ cm^{-1} for defective graphene in stage 2 with 4 nm $\lesssim L_a \lesssim$ 6 nm, and where γ_D/γ_G was seen to decrease from $\gamma_D/\gamma_G \sim 2$ to 1.4 (the range is $\gamma_D/\gamma_G \sim 3.4$ to 1.4 here) for PyCs in stage 2 with L_a in the same size regime [71]. The PyCs and A-CMNCs being in stage 2 of the amorphization trajectory is in agreement with the XRD results, which indicate that the graphitic crystallites that comprise the PyCs grow until $T_p \sim 800 - 1000$°C, at which point L_a and L_c are either constant or grow very slowly. This scaling in L_a and L_c supports the findings from Raman spectroscopy because formation of additional grain boundaries within the (100) and (110) family of planes (consistent with a growing L_a) and stacking additional (disordered) graphene-like layers on top of the (001) basal plane (consistent with a growing L_c) leads to larger defect densities that correspond to I_D/I_G and A_D/A_G increasing up to $T_p \sim 1000$°C. Also, the plateau in evolution of L_a and L_c at $T_p > 1000$°C is consistent with the results in Fig. 3b because re-organization of the defects formed at $T_p < 1000$°C [81] without further crystallite growth would lead I_D/I_G to continue to increase (since the most resonant modes dominate [84]) while A_D/A_G (representing defect probability [84]) would decrease. Additionally, although the XRD results showed a measurable impact of CNT confinement on the evolution of the L_a and L_c of the graphitic crystallites that comprise the PyCs, Raman spectroscopy, which measures differences on the atomic scales, shows no statistically significant difference between pure PyCs and A-CMNCs that is consistent with CNT confinement having little to no impact on the d_{002} evolution. This indicates that although CNT confinement could have a significant impact on the amorphization trajectory of the PyC matrix in A-CMNCs, the CNTs would need to be of smaller

diameter, as in recent reports for double-walled and single-walled CNTs [41, 42], or be of significantly higher volume fraction (*i.e.*, closer confinement of the PyC).

Chemical structure evolution

Fourier transform infrared (FTIR) spectroscopy is widely utilized to analyze the chemical structure of carbon materials [85], and representative FTIR patterns of PyCs and A-CMNCs can be found in Fig. 4. As Fig. 4 demonstrates, PyCs (Fig. 4a) and A-CMNCs (Fig. 4b) exhibit evidence of−OH stretching, which is characteristic of thermoset resins such as P-F [86] and is represented by the $\sim$ 3455 cm^{-1} and 1400 cm^{-1} bands [86, 87]. This finding for A-CMNCs is also in strong agreement with a recent report that found a significant amount of moisture adsorbed onto the surface of the CNT arrays in ambient conditions [82]. The bands at $\sim$ 2920 cm^{-1} and $\sim$ 2851 cm^{-1} correspond to sp^2 ($-CH_2$) and sp^3 ($-CH_3$) functional groups [87], and their small enhancement in relative intensity as T_p increases up to $T_p \sim 800 - 1000°C$ is consistent with the XRD results (see Fig. 2c) since such functional groups would most likely be affected by changes in the aspect ratio of the graphitic crystallites in the pure PyCs and PyC matrix of A-CMNCs. Also, Fig. 4 illustrates the presence of C=C stretching in the aromatic rings that comprise the graphitic crystallites, which is represented by the $\sim$ 1636 cm^{-1} peak [87, 88]. The broadening of the $\sim$ 1636 cm^{-1} band could also be attributed to C−O in the benzophenone groups [22]. Having both peaks around $\sim$ 1374 cm^{-1} and $\sim$ 1636 cm^{-1} could also indicate the presence of C−O stretching originating from carboxyl groups [88]. Since C−O groups are most likely present either between the layers of the graphitic crystallites, or on their edges, the evolution of the band at $\sim$ 1060 cm^{-1} (likely a result of C−O stretching [85, 87, 88]) as T_p increases is consistent with the crystallite size evolution observed by XRD (see Fig. 2c). The changes in the aromatic parts (675-900 cm^{-1}) as a function of T_p can be traced back to the proportion of −CH groups present in the condensed aromatic structures, and those found in the phenyl ring [86]. This indicates that the changes are related to the interaction between the phenolic groups, which results in further cross-linking *via* ether bridges [86]. While the bands normally ascribed to −OH, C−O, and C=C groups shown in Fig. 4b are also characteristic of pure multiwalled CNTs [89, 90], the additional $-CH_2$ and $-CH_3$ bands present in the PyC and A-CMNCs are not commonly seen in multiwalled CNTs [89, 90] meaning that they primarily exist on the graphitic crystallites that comprise the PyCs. Since Fig. 4a and Fig. 4b show a large degree of overlap between the PyC and A-CMNC FTIR pattern, these results illustrate that CNT confinement likely has very little impact on the functional groups present on the surface/edges and between the turbostratic and disordered carbon planes that comprise the crystallites in the PyC matrix of the A-CMNCs. This finding is in agreement with the XRD and Raman spectroscopy results which showed that CNT confinement does not lead to atomic-scale evolution of the PyC matrix, and additional work with CNT arrays that have an average separation on the same order of the crystallite size (*i.e.*, < 10 nm) is needed to explore if CNT proximity interactions, such as the $\pi - \pi$ interactions that lead to graphene and graphene oxide nano-scrolls [78] and highly graphitic pyrolyzed phenol-formaldehyde/graphene oxide aerogels [91, 92], can lead to re-organization of the functional groups that comprise the graphitic crystallites within the PyC matrix of A-CMNCs.

Conclusions

In summary, the influence of aligned carbon nanotube (CNT) confinement on the atomic and meso-scale evolution of the graphitic crystallites that comprise phenol-formaldehyde (P-F) derived pyrolytic carbons (PyCs) synthesized at pyrolyzation temperatures (T_p) ranging from $T_p = 600°C$ to 1400°C was quantified. CNT confinement is found to have a noticeable effect on the crystallite evolution trajectory in PyCs manufactured at $T_p \lesssim 1000°C$, however the presence of CNTs has surprisingly little impact on PyCs synthesized at $1000°C < T_p \lesssim 1400°C$. The x-ray diffraction (XRD) results indicate that aligned CNT PyC matrix nanocomposites (A-CMNCs) with a CNT volume fraction of $\sim$ 1 vol. % leads the size (L_a) of the graphitic crystallites that comprise the PyC matrix to evolve faster and reach the plateau $L_a \approx 5$ nm value at $T_p \sim 800°C$, while the baseline PyCs achieve $L_a \approx 5$ nm at a higher $T_p \sim 1000°C$, which agrees closely with recent findings on P-F derived PyCs [22]. Additionally, XRD indicates that CNT confinement in the A-CMNCs has little impact on the evolution of the thickness (L_c) and interlayer separation (d_{002}) of the graphitic crystallites that comprise the PyC matrix, which indicates that any CNT templating effects, for example through $\pi - \pi$ interactions, primarily impact crystallite growth in the basal plane family of directions. However, these interactions are not sufficient to make the crystallites more graphitic in nature since the d_{002} does not achieve $d_{002} \sim 0.3357$ nm characteristic of ideal graphite. Since the CNT confinement does not measurably impact the D- and G-band evolution of the PyC matrix as a function of T_p, Raman spectroscopy further supports the finding that

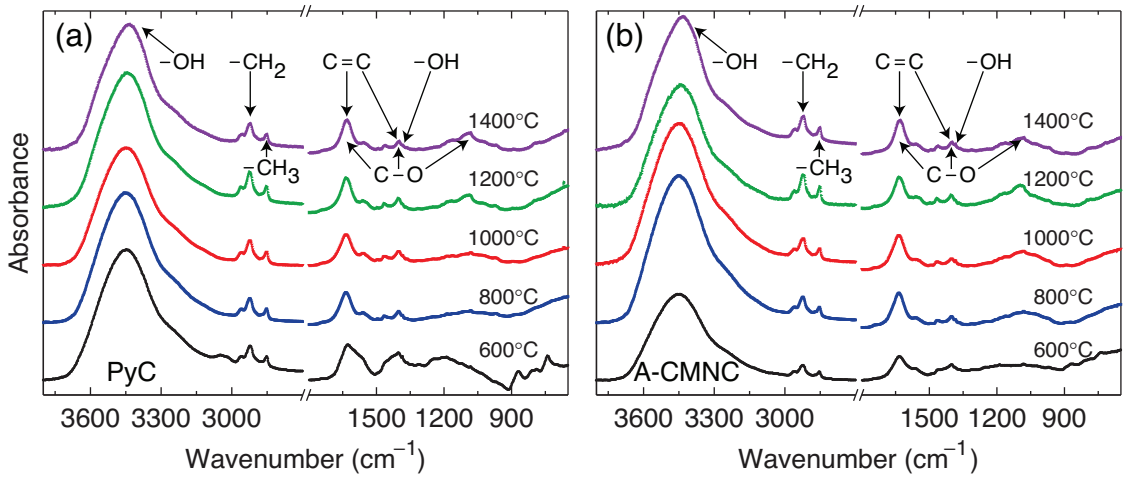

Fig. 4 FTIR spectra for pyrolysis of PyCs and A-CMNCs as a function of the pyrolysis temperature (T_p) up to $T_p = 1400°C$ showing that the chemical structure of A-CMNCs evolves slightly faster than PyCs as T_p is increased.

$\sim$ 1 vol. % aligned CNTs do not sufficiently reduce the energy barrier to facilitate the graphitization of the P-F derived PyC matrix of the A-CMNCs studied here. Additionally, the results of Fourier transform infrared (FTIR) spectroscopy also support this idea by showing that that the chemical species present in the A-CMNCs are not significantly different from those present in the baseline PyCs, which indicates that the CNT contribution is far overshadowed by functional groups present on the surface of the graphitic crystallites that comprise the PyCs. Since the evolution of the three-dimensional shape and size of pores enclosed by the crystallites that comprise the PyCs and PyC matrix of A-CMNCs are important inputs for quantifying and modeling the crystallite formation and growth mechanics as a function of CNT confinement and T_p, as well as modeling physical properties of the resulting material, but this information was not available for this study, further work *via* X-ray scattering to quantitatively map the multi-scale structure of PyCs and A-CMNCs from the atomic to micro scales following the approach of recent work [93, 94] is recommended. Because previous work showed that P-F derived PyCs perform best when manufactured at $T_p \sim 1000°C$, since this is the point at which their graphitic crystallites exhibit the highest aspect ratio (linked to enhanced hardness [22]) with the lowest sp^3 character that forms at higher T_p, CNT reinforcement could enable PyC based meta-materials to be synthesized at more widely accessible and less cost prohibitive processing temperatures below 1000°C without sacrificing mechanical performance. Because the average inter-CNT separation in the $\sim$ 1 vol. % CNT A-CMNCs studied here is $\sim$ 80 nm, but previous work has reported $\sim$ 20 vol. % CNT arrays with an average spacing $\lesssim$ 10 nm [59], further work is required on A-CMNCs with higher volume fractions of CNTs that approach the L_c of the graphitic crystallites that comprise the PyC matrix. Since P-F derived PyCs are a low density high hardness material that can already perform on the same order as diamond in aerospace structures, high volume fraction CNT A-CMNCs, where the aligned CNTs enhance or retain the original PyC hardness while significantly reducing the density, could lead to next-generation ultra-lightweight nano-architectures that outperform all currently known engineering materials.

Acknowledgements

I.Y.S. was supported in part by the Department of Defense (DoD) through the National Defense Science & Engineering Graduate Fellowship (NDSEG) Program. A.L.K. and A.J.C. were supported by the CMSE Research Experience for Undergraduates Program, as part of the MRSEC Program of the National Science Foundation under grant number DMR-08-19762, and the MIT Materials Processing Center. This work was partially supported by Airbus Group, Boeing, Embraer, Lockheed Martin, Saab AB, ANSYS, Hexcel, and TohoTenax through MIT's Nano-Engineered Composite aerospace STructures (NECST) Consortium. The authors thank P. Boisvert, T. McClure, and C. Settens for helpful discussions, and the members of necstlab at MIT for technical support and advice. This work made use of the MRSEC Shared Experimental Facilities at MIT, supported by the National Science Foundation under award number DMR-08-19762, and utilized the core facilities at the Institute for Soldier Nanotechnologies at MIT, supported in part by the U.S. Army Re-

search Office under contracts W911NF-07-D-0004 and W911NF-13-D-0001.

Compliance with ethical standards

Conflicts of interest The authors have no conflicts of interest related to this work.

Electronic supplementary material: The online version of this article (doi:10.1007/s10853-017-xxxx-x) contains supplementary material, which is available to authorized users.

References

1. Z. C. Eckel, C. Zhou, J. H. Martin, A. J. Jacobsen, W. B. Carter, T. A. Schaedler, Additive manufacturing of polymer-derived ceramics, Science 351 (2015) 58–62. doi:10.1126/science.aad2688.
2. J. Bauer, A. Schroer, R. Schwaiger, O. Kraft, Approaching theoretical strength in glassy carbon nanolattices, Nat. Mater. 15 (2016) 438–443. doi:10.1038/nmat4561.
3. C. Vakifahmetoglu, D. Zeydanli, P. Colombo, Porous polymer derived ceramics, Mater. Sci. Eng., R 106 (2016) 1 – 30. doi:10.1016/j.mser.2016.05.001.
4. D. Jang, L. R. Meza, F. Greer, J. R. Greer, Fabrication and deformation of three-dimensional hollow ceramic nanostructures, Nat. Mater. 12 (2013) 893–898. doi:10.1038/nmat3738.
5. X. Zheng, H. Lee, T. H. Weisgraber, M. Shusteff, J. DeOtte, E. B. Duoss, J. D. Kuntz, M. M. Biener, Q. Ge, J. A. Jackson, S. O. Kucheyev, N. X. Fang, C. M. Spadaccini, Ultralight, ultrastiff mechanical metamaterials, Science 344 (2014) 1373–1377. doi:10.1126/science.1252291.
6. J. Bauer, S. Hengsbach, I. Tesari, R. Schwaiger, O. Kraft, High-strength cellular ceramic composites with 3d microarchitecture, Proc. Natl. Acad. Sci. U.S.A. 111 (2014) 2453–2458. doi:10.1073/pnas.1315147111.
7. L. R. Meza, A. J. Zelhofer, N. Clarke, A. J. Mateos, D. M. Kochmann, J. R. Greer, Resilient 3d hierarchical architected metamaterials, Proc. Natl. Acad. Sci. U.S.A. 112 (2015) 11502–11507. doi:10.1073/pnas.1509120112.
8. U. G. K. Wegst, H. Bai, E. Saiz, A. P. Tomsia, R. O. Ritchie, Bioinspired structural materials, Nat. Mater. 14 (2015) 23. doi:10.1038/NMAT4089.
9. L. R. Meza, S. Das, J. R. Greer, Strong, lightweight, and recoverable three-dimensional ceramic nanolattices, Science 345 (2014) 1322–1326. doi:10.1126/science.1255908.
10. D. C. Hofmann, J.-Y. Suh, A. Wiest, G. Duan, M.-L. Lind, M. D. Demetriou, W. L. Johnson, Designing metallic glass matrix composites with high toughness and tensile ductility, Nature 451 (2008) 1085–1089. doi:10.1038/nature06598.
11. E. Munch, M. E. Launey, D. H. Alsem, E. Saiz, A. P. Tomsia, R. O. Ritchie, Tough, bio-inspired hybrid materials, Science 322 (2008) 1516–1520. doi:10.1126/science.1164865.
12. R. O. Ritchie, The conflicts between strength and toughness, Nat. Mater. 10 (2011) 817–822. doi:10.1038/nmat3115.
13. J. J. Martin, B. E. Fiore, R. M. Erb, Designing bioinspired composite reinforcement architectures via 3d magnetic printing, Nat. Commun. 6 (2015) 9641. doi:10.1038/ncomms9641.
14. M. T. Byrne, Y. K. Gun'ko, Recent advances in research on carbon nanotube-polymer composites, Adv. Mater. 22 (15) (2010) 1672–1688. doi:10.1002/adma.200901545.
15. X. Jia, Q. Zhang, M.-Q. Zhao, G.-H. Xu, J.-Q. Huang, W. Qian, Y. Lu, F. Wei, Dramatic enhancements in toughness of polyimide nanocomposite via long-cnt-induced long-range creep, J. Mater. Chem. 22 (2012) 7050–7056. doi:10.1039/C2JM15359A.
16. E. J. Siochi, J. S. Harrison, Structural nanocomposites for aerospace applications, MRS Bull. 40 (2015) 829 – 835. doi:10.1557/mrs.2015.228.
17. J. Cho, A. R. Boccaccini, M. S. P. Shaffer, Ceramic matrix composites containing carbon nanotubes, J. Mater. Sci. 44 (2009) 1934–1951. doi:10.1007/s10853-009-3262-9.
18. J. Cho, F. Inam, M. J. Reece, Z. Chlup, I. Dlouhy, M. S. P. Shaffer, A. R. Boccaccini, Carbon nanotubes: do they toughen brittle matrices?, J. Mater. Sci. 46 (2011) 4770–4779. doi:10.1007/s10853-011-5387-x.
19. Z. Gu, Y. Yang, K. Li, X. Tao, G. Eres, J. Y. Howe, L. Zhang, X. Li, Z. Pan, Aligned carbon nanotube-reinforced silicon carbide composites produced by chemical vapor infiltration, Carbon 49 (2011) 2475 – 2482. doi:10.1016/j.carbon.2011.02.016.
20. K. Kobayashi, S. Sugawara, S. Toyoda, H. Honda, An x-ray diffraction study of phenol-formaldehyde resin carbons, Carbon 6 (1968) 359 – 363. doi:10.1016/0008-6223(68)90030-4.
21. M. Shioya, T. Ojima, J. Yamashita, Activation energy of structural development for phenol formaldehyde resin-based car-

bon fibers, Carbon 39 (2001) 1869 – 1878. doi:10.1016/S0008-6223(00)00312-2.
22. I. Y. Stein, A. J. Constable, N. Morales-Medina, C. V. Sackier, M. E. Devoe, H. M. Vincent, B. L. Wardle, Structure-mechanical property relations of non-graphitizing pyrolytic carbon synthesized at low temperatures, Carbon 117 (2017) 411 – 420. doi:10.1016/j.carbon.2017.03.001.
23. M. F. L. De Volder, S. H. Tawfick, R. H. Baughman, A. J. Hart, Carbon nanotubes: Present and future commercial applications, Science 339 (2013) 535–539. doi:10.1126/science.1222453.
24. L. Liu, W. Ma, Z. Zhang, Macroscopic carbon nanotube assemblies: Preparation, properties, and potential applications, Small 7 (2011) 1504–1520. doi:10.1002/smll.201002198.
25. R. Allen, O. Ghita, B. Farmer, M. Beard, K. Evans, Mechanical testing and modelling of a vertically aligned carbon nanotube composite structure, Compos. Sci. Technol. 77 (2013) 1 – 7. doi:10.1016/j.compscitech.2013.01.001.
26. H. Cebeci, R. Guzmán de Villoria, A. J. Hart, B. L. Wardle, Multifunctional properties of high volume fraction aligned carbon nanotube polymer composites with controlled morphology, Compos. Sci. Technol. 69 (2009) 2649–2656. doi:10.1016/j.compscitech.2009.08.006.
27. D. Handlin, I. Y. Stein, R. Guzman de Villoria, H. Cebeci, E. M. Parsons, S. Socrate, S. Scotti, B. L. Wardle, Three-dimensional elastic constitutive relations of aligned carbon nanotube architectures, J. Appl. Phys. 114 (2013) 224310. doi:10.1063/1.4842117.
28. I. Y. Stein, B. L. Wardle, Mechanics of aligned carbon nanotube polymer matrix nanocomposites simulated via stochastic three-dimensional morphology, Nanotechnology 27 (2016) 035701. doi:10.1088/0957-4484/27/3/035701.
29. S. Herasati, L. Zhang, A new method for characterizing and modeling the waviness and alignment of carbon nanotubes in composites, Compos. Sci. Technol. 100 (2014) 136 – 142. doi:10.1016/j.compscitech.2014.06.004.
30. J. N. Dastgerdi, G. Marquis, M. Salimi, Micromechanical modeling of nanocomposites considering debonding and waviness of reinforcements, Compos. Struct. 110 (2014) 1 – 6. doi:10.1016/j.compstruct.2013.11.017.
31. M. Omidi, H. Rokni D. T., A. S. Milani, R. J. Seethaler, R. Arasteh, Prediction of the mechanical characteristics of multi-walled carbon nanotube/epoxy composites using a new form of the rule of mixtures, Carbon 48 (2010) 3218 – 3228. doi:10.1016/j.carbon.2010.05.007.
32. A. Pantano, P. Mantione, A numerical-analytical model for the characterization of composites reinforced by carbon nanotubes, Appl. Phys. A 99 (2010) 895–902. doi:10.1007/s00339-010-5635-y.
33. B. J. Yang, H. Souri, S. Kim, S. Ryu, H. K. Lee, An analytical model to predict curvature effects of the carbon nanotube on the overall behavior of nanocomposites, J. Appl. Phys. 116 (2014) 033511. doi:10.1063/1.4890519.
34. A. K. Naskar, J. K. Keum, R. G. Boeman, Polymer matrix nanocomposites for automotive structural components, Nat. Nanotechnol. 11 (2016) 1026–1030. doi:10.1038/nnano.2016.262.
35. B. L. Wardle, D. S. Saito, E. J. García, A. J. Hart, R. Guzmán de Villoria, E. A. Verploegen, Fabrication and characterization of ultrahigh-volume- fraction aligned carbon nanotube polymer composites, Adv. Mater. 20 (2008) 2707–2714. doi:10.1002/adma.200800295.
36. I. Y. Stein, B. L. Wardle, Morphology and processing of aligned carbon nanotube carbon matrix nanocomposites, Carbon 68 (2014) 807 – 813. doi:10.1016/j.carbon.2013.12.001.
37. R. E. Franklin, Crystallite growth in graphitizing and non-graphitizing carbons, Proc. R. Soc. London, Ser. A 209 (1951) 196–218. doi:10.1098/rspa.1951.0197.
38. F. Emmerich, Evolution with heat treatment of crystallinity in carbons, Carbon 33 (1995) 1709 – 1715. doi:10.1016/0008-6223(95)00127-8.
39. P. J. F. Harris, Structure of non-graphitising carbons, Int. Mater. Rev. 42 (1997) 206–218. doi:10.1179/imr.1997.42.5.206.
40. P. J. F. Harris, Fullerene-like models for microporous carbon, J. Mater. Sci. 48 (2013) 565–577. doi:10.1007/s10853-012-6788-1.
41. Y. Zhang, N. Tajaddod, K. Song, M. L. Minus, Low temperature graphitization of interphase polyacrylonitrile (pan), Carbon 91 (2015) 479 – 493. doi:10.1016/j.carbon.2015.04.088.
42. D. Papkov, A. M. Beese, A. Goponenko, Y. Zou, M. Naraghi, H. D. Espinosa, B. Saha, G. C. Schatz, A. Moravsky, R. Loutfy, S. T. Nguyen, Y. Dzenis, Extraordinary improvement of the graphitic structure of continuous carbon nanofibers templated with double wall carbon nanotubes, ACS Nano 7 (2013) 126–142. doi:10.1021/nn303423x.
43. G. Sui, S. Xue, H. Bi, Q. Yang, X. Yang, Desirable electrical and mechanical properties of continuous hybrid nano-scale carbon fibers containing highly aligned multi-walled

carbon nanotubes, Carbon 64 (2013) 72 – 83. doi:10.1016/j.carbon.2013.07.035.

44. H. G. Chae, M. L. Minus, A. Rasheed, S. Kumar, Stabilization and carbonization of gel spun polyacrylonitrile/single wall carbon nanotube composite fibers, Polymer 48 (2007) 3781 – 3789. doi:10.1016/j.polymer.2007.04.072.
45. H. G. Chae, Y. H. Choi, M. L. Minus, S. Kumar, Carbon nanotube reinforced small diameter polyacrylonitrile based carbon fiber, Compos. Sci. Technol. 69 (2009) 406 – 413. doi:10.1016/j.compscitech.2008.11.008.
46. K. Şahin, N. A. Fasanella, I. Chasiotis, K. M. Lyons, B. A. Newcomb, M. G. Kamath, H. G. Chae, S. Kumar, High strength micron size carbon fibers from polyacrylonitrile-carbon nanotube precursors, Carbon 77 (2014) 442 – 453. doi:10.1016/j.carbon.2014.05.049.
47. B. A. Newcomb, L. A. Giannuzzi, K. M. Lyons, P. V. Gulgunje, K. Gupta, Y. Liu, M. Kamath, K. McDonald, J. Moon, B. Feng, G. Peterson, H. G. Chae, S. Kumar, High resolution transmission electron microscopy study on polyacrylonitrile/carbon nanotube based carbon fibers and the effect of structure development on the thermal and electrical conductivities, Carbon 93 (2015) 502 – 514. doi:10.1016/j.carbon.2015.05.037.
48. Y. Han, S. Li, F. Chen, T. Zhao, Multi-scale alignment construction for strong and conductive carbon nanotube/carbon composites, Mater. Today Commun. 6 (2016) 56 – 68. doi:10.1016/j.mtcomm.2015.12.002.
49. M. B. Vázquez-Santos, E. Geissler, K. László, J.-N. Rouzaud, A. Martínez-Alonso, J. M. D. Tascón, Graphitization of highly porous carbons derived from poly(p-phenylene benzobisoxazole), Carbon 50 (2012) 2929 – 2940. doi:10.1016/j.carbon.2012.02.062.
50. C. Hu, S. Sedghi, A. Silvestre-Albero, G. G. Andersson, A. Sharma, P. Pendleton, F. R. guez Reinoso, K. Kaneko, M. J. Biggs, Raman spectroscopy study of the transformation of the carbonaceous skeleton of a polymer-based nanoporous carbon along the thermal annealing pathway, Carbon 85 (2015) 147 – 158. doi:10.1016/j.carbon.2014.12.098.
51. K. Faber, F. Badaczewski, M. Oschatz, G. Mondin, W. Nickel, S. Kaskel, B. M. Smarsly, In-depth investigation of the carbon microstructure of silicon carbide-derived carbons by wide-angle x-ray scattering, J. Phys. Chem. C 118 (2014) 15705–15715. doi:10.1021/jp502832x.
52. N. Iwashita, C. R. Park, H. Fujimoto, M. Shiraishi, M. Inagaki, Specification for a standard procedure of x-ray diffraction measurements on carbon materials, Carbon 42 (2004) 701 – 714. doi:10.1016/j.carbon.2004.02.008.
53. G. A. Zickler, B. Smarsly, N. Gierlinger, H. Peterlik, O. Paris, A reconsideration of the relationship between the crystallite size la of carbons determined by x-ray diffraction and raman spectroscopy, Carbon 44 (2006) 3239 – 3246. doi:10.1016/j.carbon.2006.06.029.
54. H. Badenhorst, Microstructure of natural graphite flakes revealed by oxidation: Limitations of {XRD} and raman techniques for crystallinity estimates, Carbon 66 (2014) 674 – 690. doi:10.1016/j.carbon.2013.09.065.
55. R. L. McCreery, Advanced carbon electrode materials for molecular electrochemistry, Chem. Rev. 108 (2008) 2646–2687. doi:10.1021/cr068076m.
56. J. Lee, I. Y. Stein, S. S. Kessler, B. L. Wardle, Aligned carbon nanotube film enables thermally induced state transformations in layered polymeric materials, ACS Appl. Mater. Interfaces 7 (2015) 8900–8905. doi:10.1021/acsami.5b01544.
57. D. S. Jacobs, Constitutive model of aligned carbon nanotube/nafion nanocomposite ionic electroactive polymer actuators, Master's thesis, Massachusetts Institute of Technology, http://hdl.handle.net/1721.1/103529 (2016).
58. J. Lee, I. Y. Stein, M. E. Devoe, D. J. Lewis, N. Lachman, S. S. Kessler, S. T. Buschhorn, B. L. Wardle, Impact of carbon nanotube length on electron transport in aligned carbon nanotube films, Appl. Phys. Lett. 106 (2015) 053110. doi:10.1063/1.4907608.
59. I. Y. Stein, B. L. Wardle, Coordination number model to quantify packing morphology of aligned nanowire arrays, Phys. Chem. Chem. Phys. 15 (2013) 4033–4040. doi:10.1039/C3CP43762K.
60. I. Y. Stein, D. J. Lewis, B. L. Wardle, Aligned carbon nanotube array stiffness from stochastic three-dimensional morphology, Nanoscale 7 (2015) 19426–19431. doi:10.1039/C5NR06436H.
61. I. Y. Stein, B. L. Wardle, Packing morphology of wavy nanofiber arrays, Phys. Chem. Chem. Phys. 18 (2016) 694. doi:10.1039/C5CP06381G.
62. H. K. Mutha, Y. Lu, I. Y. Stein, H. J. Cho, M. E. Suss, T. Laoui, C. V. Thompson, B. L. Wardle, E. N. Wang, Porosimetry and packing morphology of vertically-aligned carbon nanotube arrays via impedance spectroscopy, Nanotechnology 28 (2017) 05LT01. doi:10.1088/1361-6528/aa53aa.
63. R. R. Mitchell, N. Yamamoto, H. Cebeci, B. L. Wardle, C. V. Thompson, A technique for spatially-resolved contact resistance-free elec-

trical conductivity measurements of aligned-carbon nanotube/polymer nanocomposites, Compos. Sci. Technol. 74 (2013) 205 – 210. doi:10.1016/j.compscitech.2012.11.003.

64. I. Y. Stein, H. M. Vincent, S. A. Steiner, E. Colombini, B. L. Wardle, Processing and mechanical property characterization of aligned carbon nanotube carbon matrix nanocomposites, in: 54th AIAA Structures, Structural Dynamics, and Materials (SDM) Conference, Boston, MA, 2013. doi:10.2514/6.2013-1583.
65. I. Y. Stein, Synthesis and characterization of next-generation multifunctional material architectures: Aligned carbon nanotube carbon matrix nanocomposites, Master's thesis, Massachusetts Institute of Technology, http://hdl.handle.net/1721.1/81728 (2013).
66. I. Y. Stein, Impact of morphology and confinement effects on the properties of aligned nanofiber architectures, Ph.D. thesis, Massachusetts Institute of Technology, http://hdl.handle.net/1721.1/104126 (2016).
67. M. W. Smith, I. Dallmeyer, T. J. Johnson, C. S. Brauer, J.-S. McEwen, J. F. Espinal, M. Garcia-Perez, Structural analysis of char by raman spectroscopy: Improving band assignments through computational calculations from first principles, Carbon 100 (2016) 678 – 692. doi:10.1016/j.carbon.2016.01.031.
68. V. Tsaneva, W. Kwapinski, X. Teng, B. Glowacki, Assessment of the structural evolution of carbons from microwave plasma natural gas reforming and biomass pyrolysis using raman spectroscopy, Carbon 80 (2014) 617 – 628. doi:10.1016/j.carbon.2014.09.005.
69. A. C. Ferrari, J. Robertson, Interpretation of raman spectra of disordered and amorphous carbon, Phys. Rev. B 61 (2000) 14095–14107. doi:10.1103/PhysRevB.61.14095.
70. P. Mallet-Ladeira, P. Puech, P. Weisbecker, G. L. Vignoles, M. Monthioux, Behavior of raman d band for pyrocarbons with crystallite size in the 2−5 nm range, Appl. Phys. A 114 (2014) 759–763. doi:10.1007/s00339-013-7671-x.
71. P. Mallet-Ladeira, P. Puech, C. Toulouse, M. Cazayous, N. Ratel-Ramond, P. Weisbecker, G. L. Vignoles, M. Monthioux, A raman study to obtain crystallite size of carbon materials: A better alternative to the tuinstra-koenig law, Carbon 80 (2014) 629 – 639. doi:10.1016/j.carbon.2014.09.006.
72. X. Li, K. Li, H. Li, J. Wei, C. Wang, Microstructures and mechanical properties of carbon/carbon composites reinforced with carbon nanofibers/nanotubes produced in situ, Carbon 45 (2007) 1662 – 1668. doi:10.1016/j.carbon.2007.03.042.
73. Z. Li, C. Lu, Z. Xia, Y. Zhou, Z. Luo, X-ray diffraction patterns of graphite and turbostratic carbon, Carbon 45 (2007) 1686 – 1695. doi:10.1016/j.carbon.2007.03.038.
74. A. C. Ferrari, D. M. Basko, Raman spectroscopy as a versatile tool for studying the properties of graphene, Nat. Nanotechnol. 8 (2013) 235–246. doi:10.1038/nnano.2013.46.
75. M. S. Dresselhaus, A. Jorio, M. Hofmann, G. Dresselhaus, R. Saito, Perspectives on carbon nanotubes and graphene raman spectroscopy, Nano Lett. 10 (2010) 751–758. doi:10.1021/nl904286r.
76. A. V. Krasheninnikov, K. Nordlund, Ion and electron irradiation-induced effects in nanostructured materials, J. Appl. Phys. 107 (2010) 071301. doi:10.1063/1.3318261.
77. A. C. Ferrari, J. C. Meyer, V. Scardaci, C. Casiraghi, M. Lazzeri, F. Mauri, S. Piscanec, D. Jiang, K. S. Novoselov, S. Roth, A. K. Geim, Raman spectrum of graphene and graphene layers, Phys. Rev. Lett. 97 (2006) 187401. doi:10.1103/PhysRevLett.97.187401.
78. C. A. Amadei, I. Y. Stein, G. J. Silverberg, B. L. Wardle, C. D. Vecitis, Fabrication and chemomechanical tuning of graphene oxide nanoscrolls, Nanoscale 8 (2016) 6783. doi:10.1039/C5NR07983G.
79. F. Tuinstra, J. L. Koenig, Raman spectrum of graphite, J. Chem. Phys. 53 (1970) 1126–1130. doi:10.1063/1.1674108.
80. L. G. Cançado, K. Takai, T. Enoki, M. Endo, Y. A. Kim, H. Mizusaki, A. Jorio, L. N. Coelho, R. M. aes Paniago, M. A. Pimenta, General equation for the determination of the crystallite size L_a of nanographite by Raman spectroscopy, Appl. Phys. Lett. 88 (2006) 163106. doi:10.1063/1.2196057.
81. C. D. Latham, M. I. Heggie, M. Alatalo, S. Öberg, P. R. Briddon, The contribution made by lattice vacancies to the wigner effect in radiation-damaged graphite, J. Phys.: Condens. Matter 25 (2013) 135403. doi:10.1088/0953-8984/25/13/135403.
82. I. Y. Stein, N. Lachman, M. E. Devoe, B. L. Wardle, Exohedral physisorption of ambient moisture scales non-monotonically with fiber proximity in aligned carbon nanotube arrays, ACS Nano 8 (2014) 4591–4599. doi:10.1021/nn5002408.
83. N. Lachman, I. Y. Stein, A. Ugur, D. L. Lidston, K. K. Gleason, B. L. Wardle, Synthesis of polymer bead nano-necklaces on aligned carbon nanotube scaffolds, Nanotechnology 28 (2017) 24LT01.

doi:10.1088/1361-6528/aa71c5.

84. L. G. Cançado, A. Jorio, E. H. M. Ferreira, F. Stavale, C. A. Achete, R. B. Capaz, M. V. O. Moutinho, A. Lombardo, T. S. Kulmala, A. C. Ferrari, Quantifying defects in graphene via raman spectroscopy at different excitation energies, Nano Lett. 11 (2011) 3190–3196. doi:10.1021/nl201432g.
85. M. S. Shafeeyan, W. M. A. W. Daud, A. Houshmand, A. Shamiri, A review on surface modification of activated carbon for carbon dioxide adsorption, J. Anal. Appl. Pyrol. 89 (2010) 143 – 151. doi:10.1016/j.jaap.2010.07.006.
86. B. Strzemiecka, A. Voelkel, J. Ziôba-Palus, T. Lachowicz, Assessment of the chemical changes during storage of phenol-formaldehyde resins pyrolysis gas chromatography mass spectrometry, inverse gas chromatography and fourier transform infra red methods, J. Chromatogr. A 1359 (2014) 255 – 261. doi:10.1016/j.chroma.2014.07.045.
87. X. Lu, L. Li, B. Song, K. sik Moon, N. Hu, G. Liao, T. Shi, C. Wong, Mechanistic investigation of the graphene functionalization using p-phenylenediamine and its application for supercapacitors, Nano Energy 17 (2015) 160 – 170. doi:10.1016/j.nanoen.2015.08.011.
88. S. Biniak, A. Swiatkowski, M. Pakula, M. Sankowska, K. Kusmierek, G. Trykowski, Cyclic voltammetric and ftir studies of powdered carbon electrodes in the electrosorption of 4-chlorophenols from aqueous electrolytes, Carbon 51 (2013) 301 – 312. doi:10.1016/j.carbon.2012.08.057.
89. J. H. Lehman, M. Terrones, E. Mansfield, K. E. Hurst, V. Meunier, Evaluating the characteristics of multiwall carbon nanotubes, Carbon 49 (2011) 2581 – 2602. doi:10.1016/j.carbon.2011.03.028.
90. K. Tsirka, G. Foteinidis, K. Dimos, L. Tzounis, D. Gournis, A. S. Paipetis, Production of hierarchical all graphitic structures: A systematic study, J. Colloid Interface Sci. 487 (2017) 444 – 457. doi:10.1016/j.jcis.2016.10.075.
91. M. A. Worsley, P. J. Pauzauskie, T. Y. Olson, J. Biener, J. H. Satcher, T. F. Baumann, Synthesis of graphene aerogel with high electrical conductivity, J. Am. Chem. Soc. 132 (2010) 14067–14069. doi:10.1021/ja1072299.
92. A. Allahbakhsh, A. R. Bahramian, Self-assembled and pyrolyzed carbon aerogels: an overview of their preparation mechanisms, properties and applications, Nanoscale 7 (2015) 14139–14158. doi:10.1039/C5NR03855C.
93. E. R. Meshot, D. W. Zwissler, N. Bui, T. R. Kuykendall, C. Wang, A. Hexemer, K. J. J. Wu, F. Fornasiero, Quantifying the hierarchical order in self-aligned carbon nanotubes from atomic to micrometer scale, ACS Nano 11 (2017) 5405–5416. doi:10.1021/acsnano.6b08042.
94. H. Yue, V. Reguero, E. Senokos, A. Monreal-Bernal, B. Mas, J. Fernndez-Blzquez, R. Marcilla, J. Vilatela, Fractal carbon nanotube fibers with mesoporous crystalline structure, Carbon 122 (2017) 47 – 53. doi:10.1016/j.carbon.2017.06.032.